Hydrodynamic Changes of the Depletion Layer of Dilute Polymer Solutions Near a Wall

Juan José de Pablo and Hans Christian Öttinger
Institut für Polymere, Eidgenössische Technische Hochschule Zürich, ETH-Zentrum, 8092 Zürich, Switzerland

Yitzhak Rabin
Dept. of Chemistry, University of Southern California, Los Angeles, CA 90089

The system studied in this work is a dilute solution of rod-like molecules under simple shear flow and near a hard wall. The time evolution of the probability density function is described by a diffusion equation; particle trajectories that correspond to this equation are generated by stochastic methods. Several algorithms are presented to handle the constraints imposed by the presence of the wall. In good agreement with recent experimental work on xanthan solutions, for high shear rates we observe an increase in the thickness of the depletion layer near the wall. For low to intermediate shear rates, however, we find a transient decrease of the depletion layer thickness that has not been observed experimentally. Based on the results of our simulations, we present a simple procedure to determine a few, well defined characteristic parameters from the experimental density profiles.

Introduction

There are many practical applications in which dilute polymer solutions are subject to hydrodynamic forces. Some examples are gel permeation chromatography, enhanced oil recovery, or the flow of biological fluids in living systems. Since in most of these applications the polymer solution is confined to narrow regions of space, it is important to investigate the motion of the polymer in the vicinity of an interface and in the presence of a flow field.

Recently, Ausserré et al. (1991) have observed the existence of a depletion layer in dilute xanthan solutions subjected to simple shear flows by evanescent wave-induced fluorescence. These authors have measured the thickness variation of the depletion layer as a function of shear rate. Further, these authors present a semi-empirical explanation for the depletion-layer-thickness increase observed in their experiments.

An opposite trend was observed in recent dynamic Monte Carlo simulations for flexible polymers in shear flow, the results of which indicated that the thickness of the depletion layer decreases with increasing shear rate (Duering and Rabin, 1990, 1991). It was suggested that the discrepancy may be due to the rod-like nature of the polymers used in the experiment.

In this work, we study a dilute solution of rod-like polymers under simple shear flow. The polymer solution is represented by a rigid dumbbell immersed in a Newtonian solvent continuum. The solution is confined to a channel enclosed by two hard walls separated by a distance $2D$; the magnitude of this distance is such that the motion of a dumbbell at the center of the channel is not affected by the presence of the walls. Figure 1 shows the geometry of the system.

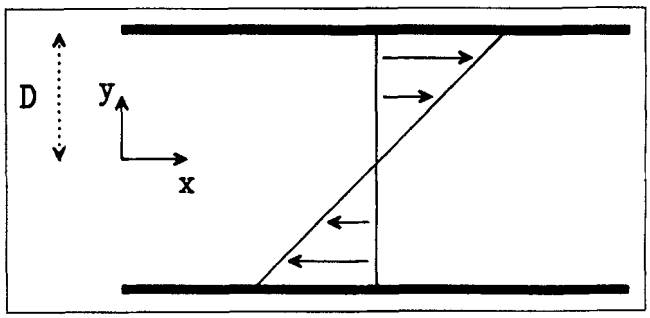

Figure 1. Geometry and coordinate system.
The rod solution flows between two hard walls moving in opposite directions and separated by a distance 2D. The origin of the coordinate system is located at the center of the channel.

Permanent address of Y. Rabin: Department of Physics, Bar-Ilan University, Ramat-Gan 59200, Israel.

The main purpose of this work has been that of developing and testing stochastic methods capable of generating particle trajectories for simplified rigid polymer models in a flow field. We have therefore concentrated our attention on rigid dumbbells in the absence of hydrodynamic interactions. In the last section of this work, however, we also present some results for multibead-rod polymers (which are very similar to rods) in the presence of bulk hydrodynamic interactions.

The time evolution of the probability density function is described by a "diffusion equation;" a stochastic method is used to generate trajectories that correspond to this equation. This numerical solution of the diffusion equation requires that time be discretized. For any finite time interval, such discretization leads to trajectories in which a dumbbell can penetrate the hard wall. Such trajectories, however, are not physical and must be rejected. It is therefore necessary to develop an integration algorithm capable of generating correct trajectories in the vicinity of a hard wall. In principle, the plates could be represented by soft walls exerting a strong force on the dumbbells; as discussed below, however, this approach introduces additional parameters into the problem. Further, the solution of the diffusion equation in the presence of these strong forces requires very small time steps and prohibitively long calculations.

We begin this work by discussing the diffusion equation for a rigid dumbbell in the vicinity of a wall. We then present two algorithms to generate the corresponding stochastic trajectories near a hard wall. We also briefly discuss a method that generates analogous trajectories in the presence of a soft, but highly repulsive, wall. After having defined some useful variables for the study of depletion layers, we compare the results of the two algorithms presented here to those for the soft wall method. Next, the diffusion equation of multibead-rod polymers in the presence of bulk hydrodynamic interactions is discussed briefly. Finally, results for the hydrodynamic properties of dilute rigid dumbbell and dilute multibead-rod solutions under pure shear flows are compared to available experimental data.

Diffusion Equation

Bird et al. (1987) extensively discuss the diffusion equation for the probability density function of a rigid dumbbell in a flow field. In this section we merely extend their diffusion equation for a rigid dumbbell in a homogeneous flow field to the case where there is a concentration gradient and therefore a dependence of the probability density function on the center-of-mass coordinates.

Let $\boldsymbol{u}$ denote a unit vector along the principal axis of the dumbbell. For a rigid-dumbbell system of homogeneous concentration, Bird et al. (1987) give the following diffusion equation for the distribution function f:

$$\frac{\partial}{\partial t} f = \frac{\partial}{\partial \boldsymbol{u}} \cdot \left(-[\boldsymbol{\kappa} \cdot \boldsymbol{u} - \boldsymbol{\kappa} : \boldsymbol{uuu}] + \frac{1}{\lambda kT} \frac{\partial \phi^{(e)}}{\partial \boldsymbol{u}} \right) f + \frac{1}{\lambda} \left(\frac{\partial}{\partial \boldsymbol{u}} \cdot \frac{\partial}{\partial \boldsymbol{u}} \right) f \quad (1)$$

$$\lambda = \frac{\zeta l^2}{2kT} \quad (2)$$

where $\phi^{(e)}$ is an external potential, k is Boltzmann's constant, T is temperature, $\boldsymbol{\kappa}$ is the transposed velocity gradient tensor, ζ is a friction coefficient, and l is the length of the rods. Note that the constant λ introduced here is six times that of Bird et al. (1987). Inertial terms and hydrodynamic interactions have been neglected to arrive at Eq. 1. In deriving Eq. 1 it was also assumed that the hydrodynamic drag is isotropic, and that the fluid velocity field is homogeneous.

The presence of walls gives rise to concentration gradients, where f depends not only on $\boldsymbol{u}$ but also on the position of the dumbbell; the corresponding diffusion equation for the distribution function becomes:

$$\frac{\partial}{\partial t} f = \underline{(1)} + \frac{\partial}{\partial \boldsymbol{r}_c} \cdot \left(-[\boldsymbol{\kappa} \cdot \boldsymbol{r}_c] + \frac{l^2}{4\lambda kT} \frac{\partial \phi^{(e)}}{\partial \boldsymbol{r}_c} \right) f + \frac{l^2}{4\lambda} \frac{\partial}{\partial \boldsymbol{r}_c} \cdot \frac{\partial}{\partial \boldsymbol{r}_c} f \quad (3)$$

where $\boldsymbol{r}_c$ denotes the position of the center of mass of the dumbbell and the term $\underline{(1)}$ denotes the righthand side of Eq. 1. The influence of walls on the motion of a dumbbell can be taken into account through the external potential.

Equation 3 is a Fokker-Planck equation. The corresponding discretized Ito stochastic differential equations for the orientation and the position of the dumbbell (Gardiner, 1985) are, respectively:

$$\boldsymbol{u}'_{i+1} = \boldsymbol{u}_i + \left([\boldsymbol{\kappa} \cdot \boldsymbol{u} - \boldsymbol{\kappa} : \boldsymbol{uuu}] - \frac{2}{\zeta l^2} \frac{\partial \phi^{(e)}}{\partial \boldsymbol{u}} \right)_i \Delta t + \frac{2}{l} \sqrt{\frac{kT}{\zeta} \Delta t}\, \boldsymbol{W}_{u,i} \quad (4)$$

and

$$\boldsymbol{r}_{c,i+1} = \boldsymbol{r}_{c,i} + \left([\boldsymbol{\kappa} \cdot \boldsymbol{r}_c] - \frac{1}{2\zeta} \frac{\partial \phi^{(e)}}{\partial \boldsymbol{r}_c} \right)_i \Delta t + \sqrt{\frac{kT}{\zeta} \Delta t}\, \boldsymbol{W}_{r,i} \quad (5)$$

where subscript i denotes quantities corresponding to time step i. The components of the vectors $\boldsymbol{W}_{u,i}$ and $\boldsymbol{W}_{r,i}$ are independent Gaussian random numbers with 0 mean and variance 1 (these components are also independent for different time steps).

For a given value of the time step Δt, particle trajectories are constructed by generating the random numbers required by the Wiener processes and then calculating the corresponding displacements according to Eqs. 4 and 5. Note that, by definition, $\boldsymbol{u}$ is a unit vector; since the random nature of Eq. 4 will yield values of $\boldsymbol{u}_{j+1}$ that are not normalized after every time step, a normalization is performed according to:

$$\boldsymbol{u}_{i+1} = \frac{\boldsymbol{u}'_{i+1}}{|\boldsymbol{u}'_{i+1}|} \quad (6)$$

It is important to point out that despite the simplicity of the normalization procedure outlined here, the fact that the construction and coupling of Eqs. 4 through 6 is equivalent to Eq 3 is nontrivial. It can be shown rigorously (Honerkamp and

Seitz, 1987), however, that Eqs. 4 through 6 coupled together are equivalent to Eq. 3.

Proposed Algorithms for a Rigid Dumbbell Near a Hard Wall

Near a wall, the discretization of time introduced in Eqs. 4 and 5 will lead to configurations in which the dumbbell penetrates the wall; since a dumbbell cannot feel the "hard" wall until it collides with it, such configurations will be particularly frequent for large time steps. To avoid overlaps between the dumbbell and the wall, the straightforward algorithm suggested by Eqs. 4 to 6 must therefore be modified when a collision occurs.

Perhaps the most straightforward way of correcting for forbidden configurations is to ignore them. In other words, if a dumbbell penetrates the hard wall, the corresponding configuration is not accepted; time is "stopped" (that is, the original configuration is counted only once for the averages), and new trial moves are attempted, starting from the original configuration of the system until an allowed position is generated. We refer to this method as the naive algorithm (N); in one dimension, it can be shown that such an algorithm leads to systematic errors of order $\sqrt{\Delta t}$ near a boundary.

A more refined algorithm can be developed by regarding the hard wall as a boundary where reflections of the underlying stochastic process take place. In analogy to the algorithms used for molecular-dynamics simulations of hard bodies, we begin by estimating the random time at which a collision takes place.

Let S_{j+1} denote the newly calculated coordinates of the dumbbell: $S=(1/2lu,r_c)$. These coordinates must be such that the two ends of the dumbbell (denoted by r_1 and r_2) are located between the two plates. If these plates are located at $-D$ and $+D$, then if the y-components of the bead positions are not in $[-D, D]$, a collision occurred in the time interval between t_j and $t_j+\Delta t$. To estimate precisely the random time at which the collision took place, we calculate the position S'_{j+1} of the dumbbell at the intermediate time $(t_j+\Delta t/2)$ according to:

$$S'_{j+1}=\left(\frac{S_{j+1}+S_j}{2}\right)+\frac{1}{2}\sqrt{\frac{kT}{\zeta}}\,\Delta t\; W_j \tag{7}$$

As for Eqs. 4 and 5, the components of W'_js are Gaussian random numbers (independent of one another and of those used for previous time steps) with 0 mean and variance 1 (Öttinger, 1990). Note that given the constraint that the original time step ended at S_{j+1}, the magnitude of the random term used to estimate the intermediate position has to be half of the original. If S'_{j+1} corresponds to an allowed configuration, then the collision occurred in the second half of the time interval between t_j and $t_j+\Delta t$. The time bisection procedure is then repeated for positions S_{j+1} and S'_{j+1}. Note that, for simplicity, we do not consider here any unobserved passages of the boundary (Öttinger, 1990). That is, S_{j+1} was reached without crossing the boundary before. If, however, S'_{j+1} corresponds to an overlapping configuration, then the collision took place in the first half of the time interval t_j and $t_j+\Delta t$. The time bisection procedure is then repeated for positions S_j and S'_{j+1}.

Several iterations are carried out until the random time of collision is estimated with the required precision. In this work, the calculated minimum reduced distance between the dumbbell and the wall must be smaller than a threshold value of 10^{-6}. Depending on the value of the time step, about 15 iterations on the average are necessary to satisfy this particular requirement.

Once the time of collision is known, the dumbbell is placed in the configuration that corresponds to that time (with one tip of the rod exactly at the wall). The dumbbell stays in such a configuration until a random fluctuation (a fluctuation corresponding to the remainder of the original full time step) moves it away from the wall. Note that only the initial and the final configurations for the full time step are considered for the averages. We refer to this algorithm as the improved (I) algorithm.

From a theoretical point of view, without correcting for unobserved reflections at the walls we should expect the improved algorithm to also give a convergence of order $\sqrt{\Delta t}$. In practice, however, convergence may be improved significantly by the presence of smaller prefactors.

Simulation of a Rigid Dumbbell Near a Soft Wall

To assess the relative merits of the algorithms discussed in the previous section, simulations were also carried out in the presence of a soft wall. Here, the soft wall is described by a potential of the form:

$$\phi^e=\pm m(y\mp D) \qquad \pm y\geq D \tag{8}$$

and

$$\phi^e=0 \qquad |y|<D \tag{9}$$

where m is the strength of the potential and y denotes the distance from the center of the channel.

In practice, the problem of choosing an adequate value of m can be circumvented to some extent by using extremely small time steps. There is, however, a limit to the value of time step that can be used for a simulation lest calculations become too long. The value of m must therefore be such that a few time steps are required for the dumbbell to leave the forbidden region.

Units and Definition of Variables

Recently, Ausserré et al. (1991) have presented experimental results for a dilute solution of a rod-like polymer near a wall and in a simple shear flow. These authors analyze their results in terms of a mean depletion layer thickness defined as:

$$\xi=-\frac{1}{\rho_b}\int_0^D[\rho(y)-\rho_b]dy \tag{10}$$

where $\rho(y)$ denotes the probability density for finding rod segments at a distance y from the center of the channel and subscript b denotes a bulk property. Our definition of probability density for Eq. 10 requires a word of caution. A scattering experiment does not probe the position of the center of mass of the rod, but rather the "segment" concentration as a

distance from the wall. We therefore calculate a scattering or "segmental" probability-density profile by dividing the width of the channel into small bins of equal size; each individual bin is then assigned an occupation number which, for a given configuration, is inversely proportional to the number of bins spanned by the y component of u. The probability-density profile obtained in this manner is denoted by $\rho(y)$.

We also define a penetration depth P according to:

$$P=\frac{1}{\rho_{cb}}\int_{(D-l/2)}^{D}\rho_c(y)dy \tag{11}$$

where subscript c denotes a center-of-mass profile (and not a segmental density profile). A penetration time is given by:

$$\tau=\frac{1}{(kT/\zeta)\rho_{cb}P}\int_{(D-l/2)}^{D}\left(y-D+\frac{l}{2}\right)^2\rho_c(y)dy \tag{12}$$

Note that since the penetration depth is calculated by integrating over the boundary layer, it provides a sensitive measure of small changes in the center-of-mass profile.

The time scale for the simulations presented in this work is set by taking $(\zeta l^2/kT)=1$. The length scale is set by taking a rod unit length ($l=1$). Parameter λ is therefore 1/2. For all the simulations shown here, we have taken the distance between the two plates as $2D=2$; we have found that for this value of channel width, the motion of the rod in the center of the channel is not affected by the presence of the walls.

Comparison of the Results of Different Algorithms

Figure 2 shows probability densities for finding the center of mass of the dumbbell at a distance r from the center of the channel. The profiles shown in Figure 2 have been calculated with the N algorithm, for $\lambda\dot{\gamma}=25$ and for several time steps. The shape of these profiles depends heavily on the size of the time step.

Figure 3 shows the center-of-mass probability density, for $\lambda\dot{\gamma}=50$, calculated with the three algorithms discussed above (N, I and SW). The results in Figure 3 correspond to the smallest time step for which each of the simulations have been performed (N, I and SW). For this shear rate, the results of the N algorithm differ significantly from those of the I and SW algorithms.

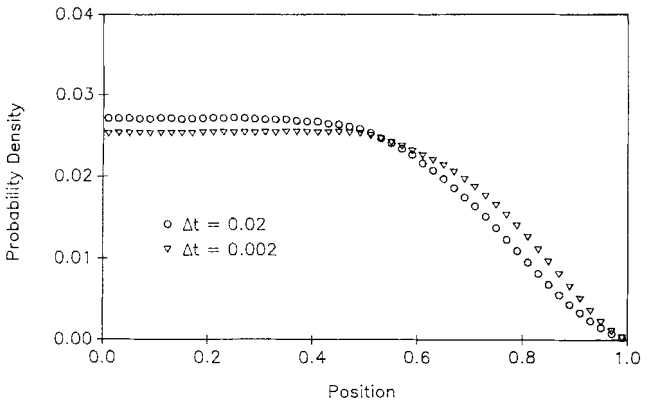

Figure 2. Center-of-mass probability density profiles calculated with the naive algorithm for $\lambda\dot{\gamma}=25$ and two different time steps.

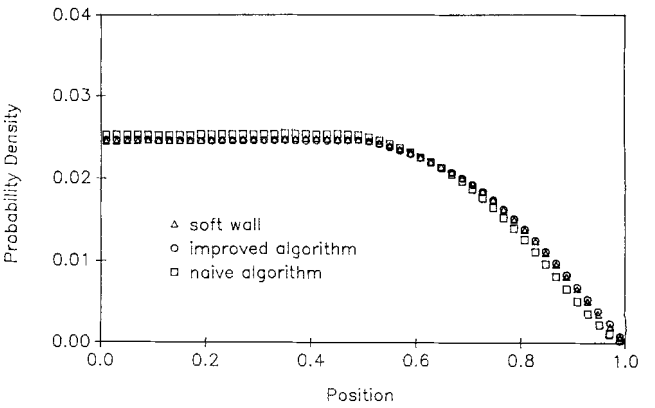

Figure 3. Center-of-mass probability density profiles calculated with the naive, improved and soft-wall algorithms for $\lambda\dot{\gamma}=25$.

The time steps used for these calculations were $\Delta t=0.0005$, $\Delta t=0.0005$, and $\Delta t=0.0001$, respectively.

Figure 4 shows the time-step dependence of the penetration depth calculated by the N and the I algorithms, also for $\lambda\dot{\gamma}=25$. The results of the N algorithm depend significantly on the size of the time step; these results exhibit a $\sqrt{\Delta t}$ dependence. The results of the I algorithm depend only very slightly on time step, and extrapolations to the zero-time-step limit can be carried out with confidence. Further, the convergence of the I algorithm could be further improved by resorting to additional refinements discussed by Öttinger (1990). As pointed out earlier, we expect the convergence of the improved algorithm also to be of order $\sqrt{\Delta t}$; this convergence, however, is improved significantly (with respect to the naive algorithm) by the presence of a much smaller prefactor.

Table 1 gives the average time spent by the dumbbell both in the depletion zone and in the bulk along with a measure of

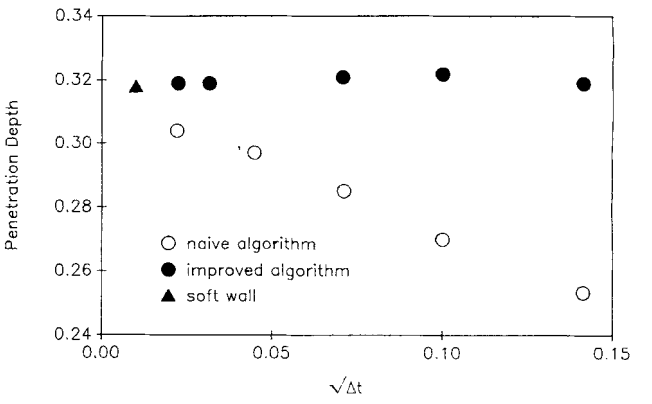

Figure 4. Time-step dependence of the calculated mean depletion-layer thickness for the naive and the improved algorithms.

Figure 4 also shows a small-time-step result for the soft-wall algorithm. The shear rate for all calculations was $\lambda\dot{\gamma}=25$.

Table 1. Variables and System Properties Calculated with Various Algorithms

$\lambda\dot{\gamma}$	A	Δt	$\langle u_y \rangle$	T_d	ξ	P	τ
0.5	I	10^{-2}	0.1718(4) 0.3319(1)	34	0.237(5)	0.259(1)	0.0421
5	I	10^{-3}	0.1509(3) 0.274(1)	35	0.223(5)	0.275(1)	0.0436
25	S	10^{-4}	0.125(9) 0.159(1)	38	0.189(20)	0.311(4)	0.0469
25	N	5×10^{-4}	0.1039(3) 0.1593(2)	37	0.202(6)	0.300(2)	0.0447
25	I	5×10^{-4}	0.1062(2) 0.1588(3)	38	0.189(3)	0.312(1)	0.0474
50	I	2.5×10^{-4}	0.0877(1) 0.1218(4)	39	0.181(8)	0.320(2)	0.0494
250	I	5×10^{-5}	0.0546(1) 0.0660(2)	37	0.202(10)	0.295(2)	0.0481
500	I	2.5×10^{-5}	0.0460(1) 0.0529(1)	34	0.235(20)	0.263(3)	0.0445
1,000	I	10^{-5}	0.0359(4) 0.0398(1)	31	0.273(28)	0.227(5)	0.0383
1,500	I	5×10^{-6}	0.0329(2) 0.0357(1)	29	0.291(26)	0.207(5)	0.0333
2,500	I	5×10^{-6}	0.0275(2) 0.0286(1)	26	0.321(36)	0.178(4)	0.0273
3,500	I	4×10^{-6}	0.0248(2) 0.0254(1)	24	0.334(40)	0.163(5)	0.0230

A = algorithm (I = improved, S = soft-wall, N = naive)
Δt = time step
$\langle u_y \rangle$ = average y component of u in the depletion region and in the bulk
T_d = percentage of time spent in depletion region
ξ = mean depletion-layer thickness
P = penetration depth
τ = penetration time

the respective orientations (expressed as the average y component of the rod vector u). Here, the depletion zone is simply defined as the region within 0.5 of the wall (the dumbbell has unit length). Table 1 also gives the mean depletion-layer thickness, the penetration depth, and the penetration time. The time spent by the dumbbell in the depletion layer is smaller for the N algorithm than for the I and SW algorithms; the corresponding mean depletion-layer thickness is also larger. The average orientation of the dumbbell is similar for all algorithms. While the differences are not large, these results show decisively that the improved algorithm is superior to the naive algorithm.

The CPU time required for the calculations presented here depends on the time step and therefore on the shear rate. For the highest shear rates discussed here, a typical simulation run with the improved algorithm takes on the order of several hours on a workstation.

Rigid Multibead-Rod Polymers

So far, our discussion has been focused on the behavior of rigid dumbbells in the absence of hydrodynamic interactions. In principle, however, a rod-like polymer resembles more closely a rigid multibead-rod model than a rigid dumbbell. Further, the presence of hydrodynamic interactions between different beads give rise to a nonisotropic drag which might have a significant effect on the properties of the solution.

Bird and Curtiss (1984) have described a detailed kinetic theory for dilute solutions of rigid multibead-rod polymers. Here, we have merely extended their discussion to the case where the concentration profile is nonuniform (see Appendix A). Following their work, we arrive at the following discretized Ito stochastic differential equations for the center of mass and for the rod vector of a multibead-rod polymer solution:

$$r_{c,i+1} = r_{c,i} + [\kappa \cdot r_c]\Delta t + \sqrt{\frac{2kT}{\zeta C_\delta}\Delta t}\left(\delta - \left(1 - \frac{1}{\sqrt{1-(C_{uu}/C_\delta)}}\right)uu\right)_i \cdot W_{r,i} \quad (13)$$

$$u'_{i+1} = u_i + ([\kappa \cdot u] - [\kappa : uuu])_i \Delta t + \frac{2}{l}\sqrt{\frac{2kT}{\zeta C_\delta}\Lambda\Delta t}\, W_{u,i} \quad (14)$$

where C_δ, C_{uu} and Λ are numerical coefficients (described in Appendix A).

Equations 13 and 14 are for a rigid multibead-rod model with hydrodynamic interactions. The derivation of these equations is given in Appendix A. In the large N limit, an integral-equation approximation can be made to arrive at similar expressions. Such an approach is briefly discussed in Appendix B.

Here, we only present results for $h = 0.25$ and for a 100-bead rod. To facilitate comparison between rigid multibead rod results and rigid dumbbell results, constant C_δ is fixed at a value of 2 (all other constants are the same as in the dumbbell simulations discussed above). These are typical values of the parameters for the study of rod dynamics in solution. The stochastic trajectories corresponding to Eqs. 13 and 14

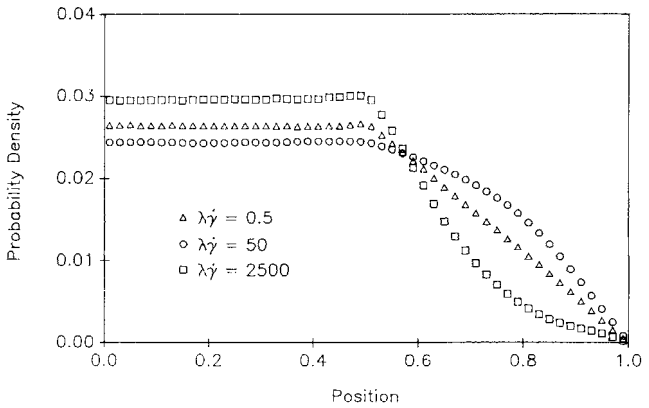

Figure 5. Center-of-mass probability density profiles calculated with the improved algorithm for $\lambda\dot{\gamma} = 0.5$, $\lambda\dot{\gamma} = 50$, and $\lambda\dot{\gamma} = 2{,}500$.

The time steps used for these calculations were $\Delta t = 0.01$, $\Delta t = 0.00025$, and $\Delta t = 0.000005$, respectively.

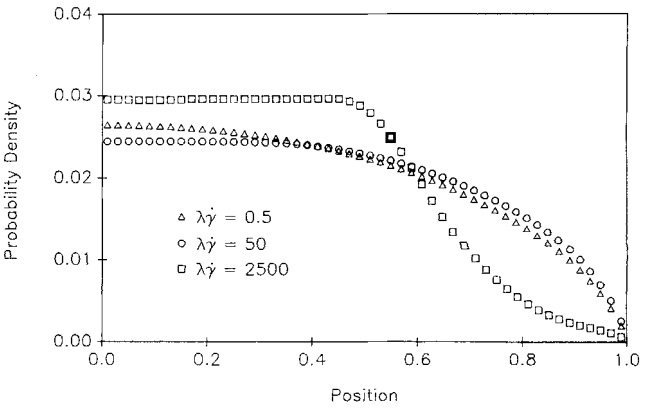

Figure 6. Segmental probability density profiles calculated with the improved algorithm.

Same conditions as Figure 5

are generated according to the prescription outlined above for the simulation of rigid dumbbells.

Results and Discussion

Figure 5 shows center-of-mass profiles calculated for different shear rates with the *I* algorithm. At low shear rates ($\lambda\dot{\gamma} = 1/2$), the profile is essentially that of a dumbbell solution at equilibrium (no flow). At moderate shear rates (such as $\lambda\dot{\gamma} = 50$), the probability of finding the dumbbell in the depletion layer region is higher than at low shear rates; there is a corresponding decrease of the depletion layer thickness and an increase of the penetration time. At high shear rates (such as $\lambda\dot{\gamma} = 2{,}500$), the probability of finding the dumbbell in the depletion layer is lower than for both the low and the moderate-shear-rate regimes. Figure 6 shows the corresponding segmental probability density profiles.

These findings are explained by the fact that at moderate shear rates a dumbbell tends to align itself with the direction of the flow, and therefore its center of mass can approach the wall more closely than in the no-flow case. The characteristic time for a full rotation is greater than the time for the dumbbell to diffuse into the depletion layer region. The average orientation of the dumbbell in the depletion layer differs significantly from that in the bulk (the average y component of $\boldsymbol{u}$ is smaller in the depletion layer). At higher shear rates, however, the rotation time becomes smaller; as soon as a dumbbell starts diffusing into the depletion layer region, a rotation takes place and kicks it back to the bulk region. The average orientations of the dumbbell in the depletion layer and in the bulk are very similar. As postulated by Ausserré et al. (1991), at very high shear rates the dumbbell is expected to rotate so fast that it can be envisioned as a sphere that cannot approach the wall closer than a distance equal to its radius.

In their scattering measurements, Ausserré et al. (1991) do not observe the transient decrease of the depletion layer thickness that we find here. These authors, however, do not report enough measurements in the low-to-moderate shear rate regimes to conclude that this decrease does not occur. Further, these authors also report that for depletion-layer thicknesses lower than the minimum wave-length of their experiments ($\Lambda_{min} \approx 30$ nm), their measurements become inaccurate. For a rod-length around 350 nm and for $\lambda\dot{\gamma} = 50$, we estimate a depletion-layer thickness around 60 nm; under such conditions, we do not know if the experimental procedure employed by Ausserré et al. (1991) would have the accuracy required to detect the decrease of the depletion layer predicted by our models for the moderate shear-rate regime.

It is important however, to recognize that while the shape of the center-of-mass probability density profile for $\lambda\dot{\gamma} = 50$ differs significantly from that for $\lambda\dot{\gamma} = 1/2$, the differences between the corresponding segmental density profiles are not very pronounced. Since these differences are actually very small (and since the method of Ausserré et al., 1991, samples density profiles), they would be difficult to detect experimentally (if they occur at all). The fact that these differences are small is also shown in Table 1. At intermediate shear rates, the center of mass of a dumbbell can approach the wall more closely than at high shear rates. For such shear rates, however, the average y component of the rod vector is smaller (particularly in the depletion region) than for the low shear rates. A closer approach of the center of mass to the wall is therefore compensated by a change in the respective orientations of a dumbbell, thereby giving rise to segmental density profiles which are not too different from each other.

Ausserré et al. (1991) assume that in the high-shear-rate regime, the depletion layer region is almost completely inaccessible to the rods; they therefore consider a step-like center-of-mass profile to deduce a rod length from their scattering measurements. Figure 6, however, shows that even for the highest shear rates studied here the center-of-mass profiles are not step functions. Assume that a step-like profile could therefore lead to an unnecessary loss of accuracy in the study of depletion layers, in particular, in the estimation of a rod length.

A first-order correction to a step profile can be obtained by assuming that the center-of-mass profile is uniform in the interval $[-B,B]$, with $B = D - l/2 + P$, only at time 0. Such a profile can be represented by a sum of delta functions that describe the possible positions of the center of mass of the rod. As time evolves, the delta functions spread as Gaussian functions according to a purely diffusive process; a corrected center-of-mass profile can therefore be inferred from the sum

of these Gaussians at time τ' (which is an adjustable parameter). If the penetration time τ defined in Eq. 12 corresponds to the characteristic time for diffusion of the center of mass of the rod into the depletion layer, then we could expect to find a simple relationship between parameter τ' and time τ. The Gaussian functions are given by (Gardiner, 1985):

$$\rho_{ci}(y, \tau) = \frac{1}{\sqrt{2\pi(kT/\zeta)\tau'}} \exp\left[-\frac{(y-y_i)^2}{2(kT/\zeta)\tau'}\right] \quad (15)$$

where y_i's are the positions of the delta functions at time 0. After integrating over y_i (in the interval $[-B,B]$), the center-of-mass profile at time τ' is approximated by:

$$\rho_c(y, \tau') \simeq \frac{1}{4B}\left[\operatorname{erf}\left(\frac{y+B}{\sqrt{2(kT/\zeta)\tau'}}\right) - \operatorname{erf}\left(\frac{y-B}{\sqrt{2(kT/\zeta)\tau'}}\right)\right] \quad (16)$$

where erf denotes the error function. If, for a given shear rate, P is taken from Table 1, and τ' is taken to be equal to $\tau/2$ (τ is also given in Table 1), then the center-of-mass profile calculated from Eq. 16 is in reasonable agreement with simulation.

Figure 7 shows the simulated segmental profile for $\lambda\dot{\gamma} = 2{,}500$ and the corresponding step-like profile. It also shows the analytical profile calculated according to Eq. 16. The improvement of the "diffuse" profile over the step profile suggests that Eq. 16 could be applied in practice to deduce some important, well-defined variables from the experimental profiles.

Equation 16 is in essence a two-parameter expression: one parameter corresponds to B, and the other corresponds to $(\tau' kT/\zeta)$. If, for high shear rates, Eq. 16 is inserted into the righthand side of Eq. 11, it can be seen that parameter B is indeed $D - l/2 + P$. If Eq. 16 is inserted into the righthand side of Eq. 12, we find that $\tau = \tau' + P^2\zeta/3kT$. For $\tau = 2\tau'$ (which was found to be successful in fitting the simulation results), this equality implies that $P^2 \approx 3kT\tau/2\zeta$; this approximate relationship is confirmed by the data in Table 1.

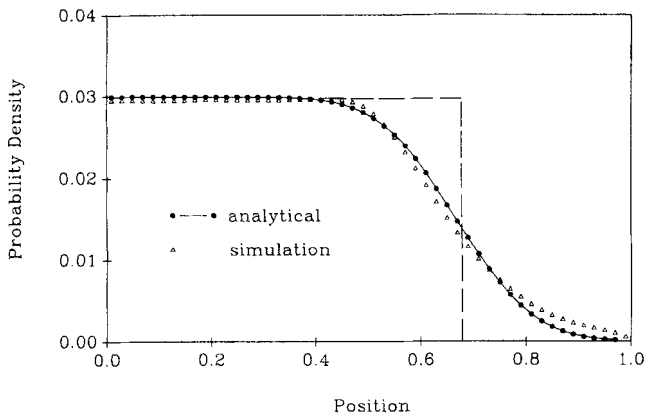

Figure 7. Center-of-mass probability density profiles for $\lambda\dot{\gamma} = 2{,}500$.

The open triangles show simulation results. The dotted line shows a step-like profile. The solid line shows the profile calculated with Eq. 16 with parameters given in Table 1.

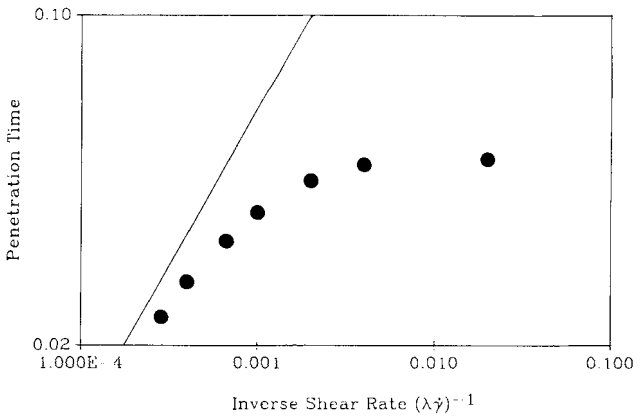

Figure 8. Penetration time vs. inverse shear rate.

The solid symbols show simulation results. The solid line, shown only for comparison, has a slope of 2/3.

It can be shown from steady-state considerations (Öttinger, 1988) that, for high shear rates, the rotation period for the rod in a shear flow is proportional to the $(-2/3)$ power of the shear rate. In this respect, we disagree with Ausserré et al. (1991), whose theoretical discussion of the motion of a rod in a simple shear flow implies, at high shear rates, an inverse power dependence of the rotation period on shear rate. We have tried to confirm this power-law behavior from our simulation data, but the accuracy of our results at high shear rates does not allow a precise determination of the exponent. Table 1 gives the calculated penetration time for the rod at different shear rates. Figure 8 shows on a logarithmic scale these penetration times as a function of shear rate. For comparison, a line of slope (2/3) has been drawn on the same figure. Despite the uncertainty of our results, it appears that the penetration time approaches indeed the expected $(-2/3)$-power law behavior at high shear rates.

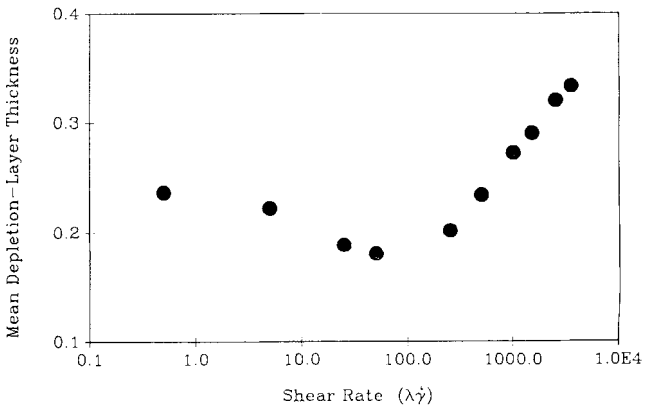

Figure 9. Mean depletion layer thickness as a function of shear rate for a dilute solution of rigid dumbbells and in the absence of hydrodynamic interactions.

The solid symbols show simulation results.

Table 2. Variables and System Properties for a Multibead Rod of 100 Beads and with Hydrodynamic Interaction ($h = 0.25$)

$\lambda\dot{\gamma}$	A	Δt	$\langle u_y \rangle$	T_d	ξ	P	τ
5	I	10^{-3}	0.1653(3) 0.3151(9)	34	0.233(5)	0.264(3)	0.0423
25	I	10^{-4}	0.1321(6) 0.2123(3)	37	0.210(31)	0.290(5)	0.0446
25	I	2.5×10^{-5}	0.1334(9) 0.2152(9)	36	0.220(24)	0.283(5)	0.0445
50	I	10^{-4}	0.1132(9) 0.1669(9)	37	0.203(19)	0.297(5)	0.0460
250	I	5×10^{-5}	0.0716(6) 0.0898(5)	36	0.221(15)	0.280(3)	0.0468
500	I	2.5×10^{-5}	0.0589(4) 0.0707(1)	33	0.253(17)	0.249(5)	0.0436
1,000	I	2.5×10^{-5}	0.0485(3) 0.0550(2)	30	0.291(14)	0.212(3)	0.0376
2,500	I	10^{-5}	0.0369(1) 0.0398(1)	25	0.339(19)	0.164(3)	0.0268

Figure 9 shows the depletion layer thickness as a function of shear rate. As discussed above, after a transient decrease for low to moderate shear rates, ξ increases for high shear rates. The increase in ξ observed here for values of $(\lambda\dot{\gamma})$ above 250 is consistent with the experimental findings of Ausserré et al. (1991).

The transient decrease of ξ observed for the rigid dumbbells in the low-to-intermediate shear-rate regime can also be detected in the results for multibead rods. Table 2 gives results for the rigid multibead-rods of 100 beads (for $h = 0.25$). Figure 10 shows the depletion layer as a function of shear rate. For multibead rods, the drag in the direction of the rod vector can be twice as large as the drag in the direction perpendicular to it. It would therefore be natural to expect the minimum in the depletion layer thickness to be less pronounced. This is not the case, and the minimum is almost as pronounced as for the rigid dumbbells.

It is important to emphasize some of the approximations and simplifications implicit in the models studied here. Improvement of these approximations could in turn lead to further research in this area and to more accurate studies of rod dynamics near boundaries. Perhaps the main simplification has been that of assuming a uniform flow field. As the results show, the concentration of the polymer near the wall is much smaller than in the bulk; this should lead to nonuniform flow fields. A second approximation has been that of neglecting hydrodynamic forces caused by the rotation of the rods around their main axis. A third approximation has been that of neglecting the modification of hydrodynamic interactions created by the presence of the wall. These are all questions that should be addressed in future work.

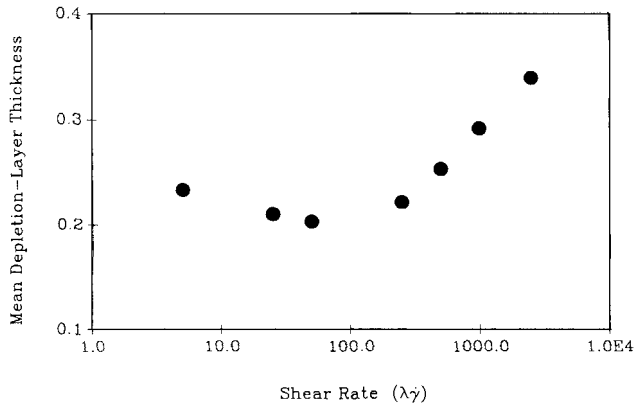

Figure 10. Mean depletion layer thickness as a function of shear rate for a dilute solution of multibead-rod rigid polymers with bulk hydrodynamic interactions.

The solid symbols show results of simulations of particles of 100 beads and with hydrodynamic interaction parameter $h = 0.25$.

Acknowledgment

The authors are indebted to Ulrich Suter for helpful discussions and for encouraging the collaboration that resulted in this work. H. C. Öttinger is grateful to the Swiss National Foundation for Scientific Research (grant No. 21-29571.90) for financial support.

Literature Cited

Ausserré, D., J. Edwards, J. Lecourtier, H. Hervet, and F. Rondelez, "Hydrodynamic Thickening of Depletion Layers in Polymer Solutions," *Europhys. Lett.*, **14**, 33 (1991).

Bird, R. B., and C. F. Curtiss, "Kinetic Theory and Rheology of Solutions of Rigid Rodlike Macromolecules," *J. Non-Newt. Fluid. Mech.*, **14**, 85 (1984).

Bird, R. B., C. F. Curtiss, R. C. Armstrong, and O. Hassager, *Dynamics of Polymeric Liquids*, Vol. 2, Wiley, New York (1987).

Duering, E., and Y. Rabin, "Polymers in Shear Flow near Repulsive Boundaries," *Macromol.*, **23**, 2232 (1990).

Duering, E., and Y. Rabin, "Polymers in Plane Poiseuille Flow: Dynamic Monte Carlo Simulation," *J. Rheol.*, **35**, 213 (1991).

Gardiner, C. W., *Handbook of Stochastic Methods*, 2nd Ed., Springer-Verlag, Heidelberg (1985).

Honerkamp, J., and R. Seitz, "Transient Behavior of Liquid Crystalline Polymers," *J. Chem. Phys.*, **87**, 3120 (1987).

Öttinger, H. C., "A Note on Rigid Dumbbell Solutions at High Shear Rates," *J. Rheol.*, **32**, 135 (1988).

Öttinger, H. C., "Simulation Algorithm for Reptation Theories Yielding Viscometric Functions Without Errors Due To Time Discretization," *Computer Simulation of Polymers*, R. J. Roe, ed., Prentice-Hall, Englewood Cliffs, NJ (1990).

Riseman, J., and J. G. Kirkwood, "The Intrinsic Viscosity, Translational and Rotatory Diffusion Constants of Rod-Like Macromolecules in Solution," *J. Chem. Phys.*, **18**, 512 (1950).

APPENDIX A

We follow the work of Bird and Curtiss (1984) to arrive at

a "diffusion equation" for dilute multibead-rod rigid polymer solutions of nonuniform concentration. Our notation closely follows that of these authors. Consider a rigid multibead rod of N beads separated by a distance a from each other [$l=(N-1)a$]. For odd N, the beads are labeled by even integers from $-(N-1)$ to $(N-1)$; for even N, the beads are labeled by odd integers from $-(N-1)$ to $(N-1)$. The hydrodynamic forces acting on the beads are taken into account through an Oseen-Burgers tensor (Bird et al., 1987). The motion of the beads produces a perturbation of the velocity at the position of bead ν given by:

$$v' = -\sum_{\mu=-(N-1)}^{N-1} [\Omega_{\nu\mu}\cdot F_{\mu}^{(h)}] \tag{A1}$$

in which summation is over all beads except for $\mu=\nu$. In Eq. A1, $\Omega_{\nu\mu}$ denotes the hydrodynamic interaction tensor. The Oseen-Burgers expression for this tensor is:

$$\Omega_{\nu\mu}=\frac{(1-\delta_{\nu\mu})}{8\pi\eta_s(a/2)}\frac{1}{|\nu-\mu|}(\delta+uu) \tag{A2}$$

An expression for the hydrodynamic forces is obtained by combining Eqs. A1 and A2, and then invoking Stokes' law:

$$F_{\nu}^{(h)} = -\zeta([\![\dot{r}_c]\!]-v_0-[\kappa\cdot r_c])-\zeta\frac{a}{2}\nu([\![\dot{u}]\!]-[\kappa\cdot u]) - 2h\sum_{\mu}\frac{(\delta+uu)\cdot F_{\mu}^{(h)}}{|\nu-\mu|} \tag{A3}$$

where the hydrodynamic interaction parameter is $h=\zeta/(8\pi\eta_s a)$, and the double brackets denote a momentum-averaged quantity. The velocity $(v_0+[\kappa\cdot r_c])$ corresponds to the imposed homogeneous flow field at the center of mass. For notational convenience, we define:

$$J_1=\zeta([\![\dot{r}_c]\!]-v_0-[\kappa\cdot r_c]) \tag{A4}$$

$$J_2=\zeta([\![\dot{u}]\!]-[\kappa\cdot u]+[\kappa{:}uuu]) \tag{A5}$$

The hydrodynamic force on bead ν can be decomposed into components along the rod axis and perpendicular to it:

$$[uu\cdot F_{\nu}^{(h)}] = -[uu\cdot J_1]+\zeta\frac{a}{2}\nu\,[\kappa{:}uuu]-4h\sum_{\mu}\frac{uu\cdot F_{\mu}^{(h)}}{|\nu-\mu|} \tag{A6}$$

$$[(\delta-uu)\cdot F_{\nu}^{(h)}] = -[(\delta-uu)\cdot J_1] - \frac{a}{2}\nu J_2 - 2h\sum_{\mu}\frac{(\delta-uu)\cdot F_{\mu}^{(h)}}{|\nu-\mu|} \tag{A7}$$

Equations A6 and A7 can be expressed in the form:

$$\phi_{\nu}(\alpha)+2\alpha\sum_{\mu}\frac{\phi_{\mu}(\alpha)}{|\nu-\mu|}=\frac{1}{2}\nu-C \tag{A8}$$

where either

$$\phi_{\nu}(\alpha)=\frac{uu\cdot F_{\nu}^{(h)}}{\zeta a[\kappa{:}uuu]};\quad \alpha=2h$$

or

$$\phi_{\nu}(\alpha)=-\frac{(\delta-uu)\cdot F_{\nu}^{(h)}}{aJ_2};\quad \alpha=h$$

Equation A8 can also be expressed in matrix form as:

$$M\hat{\Phi}=\frac{1}{2}\hat{v}-C\hat{\delta}$$

where $\hat{\Phi}$ is a vector with components ϕ_{ν}, $\hat{v}$ is a vector with components ν, and $\hat{\delta}$ is a column vector with unit components. This matrix equation can be solved to yield the components of $F_{\nu}(h)$ (Eq. A8) in the directions along the rod axis and perpendicular to it. The expressions for ϕ have the general form:

$$\phi_{\nu}(\alpha)=A_{\nu}(\alpha)-B_{\nu}(\alpha)C \tag{A9}$$

where the A's and B's satisfy the symmetry relations $A_{\nu}=-A_{-\nu}$ and $B_{\nu}=B_{-\nu}$.

To obtain an equation for the motion of the center of mass, the newly derived components of the hydrodynamic forces are used in a total force balance which, in the absence of external forces, becomes:

$$\sum_{\nu}F_{\nu}^{(h)}+\sum_{\nu}F_{\nu}^{(b)}=0 \tag{A10}$$

where superscript (b) denotes the Brownian forces acting on the beads. Note that the sum of all constraint forces vanishes. The result of these manipulations is:

$$J_1=-\frac{kT}{C_{\delta}}\left[\delta+\frac{(C_{uu}/C_{\delta})}{1-(C_{uu}/C_{\delta})}uu\right]\cdot\frac{\partial}{\partial r_c}\ln f \tag{A11}$$

where

$$C_{\delta}=\sum_{\nu}B_{\nu}(h) \tag{A12}$$

$$C_{uu}=\sum_{\nu}B_{\nu}(h)-\sum_{\nu}B_{\nu}(2h) \tag{A13}$$

The part of the diffusion equation that generates the Ito stochastic differential equation (ISDE) for the center of mass is therefore:

$$\frac{\partial}{\partial r_c}\cdot[\![\dot{r}_c]\!]f=\frac{\partial}{\partial r_c}\cdot[\kappa\cdot r_c]-\frac{kT}{\zeta C_{\delta}}\frac{\partial}{\partial r_c}\cdot\left[\delta+\frac{(C_{uu}/C_{\delta})}{1-(C_{uu}/C_{\delta})}uu\right]\cdot\frac{\partial}{\partial r_c}f \tag{A14}$$

where, without loss of generality, we have set $v_0=0$. The cor-

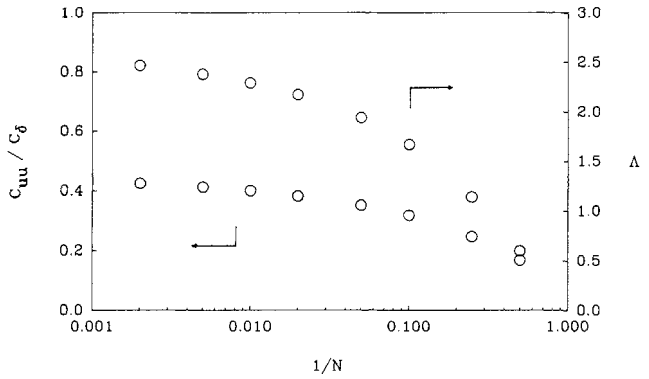

Figure A1. Parameters C_{uu}/C_δ and Λ (appearing in the equations of motion for multibead-rod rigid polymers) as a function of number of beads for $h=0.25$.

responding discretized ISDE for the position of the rod is therefore:

$$r_{c,i+1}=r_{c,i}+[\kappa\cdot r_c]\Delta t + \sqrt{\frac{2kT}{\zeta C_\delta}\Delta t}\left(\delta-\left(1-\frac{1}{\sqrt{1-(C_{uu}/C_\delta)}}\right)uu\right)_i\cdot W_{r,i} \quad \text{(A15)}$$

where the components of $W_{r,i}$ are Gaussian random numbers with ϕ mean and variance 1.

The derivation of an equation for the rod-vector motion is given in detail by Bird and Curtiss (1984). Here, it suffices to quote the necessary equations to arrive at the required ISDE for u. The part of the diffusion equation that generates the desired ISDE is given by:

$$\frac{\partial}{\partial u}\cdot[[\dot{u}]]f=-\frac{1}{\lambda_N(h)}\left(\frac{\partial}{\partial u}\cdot\frac{\partial}{\partial u}f\right)-\left(\frac{\partial}{\partial u}\cdot[\kappa\cdot u]-[\kappa:uuu]f\right) \quad \text{(A16)}$$

where

$$\lambda_N(h)=\frac{\zeta a^2}{kT}\left(\sum_\nu \frac{1}{2}\nu A_\nu(h)\right) \quad \text{(A17)}$$

The ISDE for the rod vector is therefore:

$$u'_{i+1}=u_i+([\kappa\cdot u]-[\kappa:uuu])\Delta t+\frac{2}{l}\sqrt{\frac{2kT}{\zeta C_\delta}\Lambda\Delta t}\,W_{u,i} \quad \text{(A18)}$$

where

$$\Lambda=\frac{C_\delta(N-1)^2}{2\sum_\nu \nu A_\nu(h)} \quad \text{(A19)}$$

Figure A1 shows the ratio C_{uu}/C_δ (appearing in the ISDE for the position of the rod) and parameter Λ (appearing in the ISDE for the orientation of the rod) as a function of the number of beads for $h=0.25$. To compare the results for the rigid dumbbells to those for the multibead rods, we arbitrarily fix C_δ at 2 (which corresponds to a particularly useful convection for the basic time scale).

Appendix B

An alternative approach to the matrix methods described in Appendix A can be taken to arrive at the large N limit of the diffusion equation. Following Risemann and Kirkwood (1950), for large N the sum appearing in Eq. A9 is replaced by an integral equation:

$$\phi(x)=\frac{1}{2}Nx-C+2\alpha\int_{-1}^{1}K(x,y)\phi(y)dy \quad \text{(B1)}$$

where

$$x=\frac{\nu}{N};\qquad y=\frac{\mu}{N}$$

$$K(x,y)=1/(x-y);\qquad -1\le y\le x-1/N$$
$$=0;\qquad x-1/N\le y\le x+1/N$$
$$=1/(y-x);\qquad x+1/N\le y\le 1$$

Riseman and Kirkwood (1950) give a solution of the form:

$$\phi(x)=-\frac{C}{\rho_0}+\sum_{k=-\infty}^{k=+\infty}{}'\frac{1}{1-4\alpha Ci(|k|\pi/n)}\left(g_k+\left(\frac{\rho_k}{\rho_0}\right)C\right)e^{i\pi kx} \quad \text{(B2)}$$

where the prime on the sum indicates $k\neq 0$, and

$$\rho_0=1-4\alpha[1-\ln(2N)]$$

$$\rho_k=\frac{1}{2}\int_{-1}^{1}(1+2\alpha\ln[N^2(1-x^2)])e^{i\pi kx}dx$$

$$g_k=\frac{Ni}{k\pi}(-1)^{k+1};\qquad k>0$$

$$Ci(x)=\int_\infty^x\frac{\cos t}{t}dt$$

The summations in the force balance appearing in Eq. A12 are now replaced with integrals; the result for the sum of hydrodynamic forces acting on the beads is:

$$\int_{-1}^{1}\phi(x)dx=-\frac{2C}{1+4\alpha\ln N+4\alpha(\ln 2-1)}$$

With this result, the equation of motion for the center of mass of the rod in the large N limit becomes:

$$[[\dot{r}_c]] = [\kappa \cdot r_c] - \frac{kTC_{r2}}{\zeta}\left[\delta + \left(\frac{C_{r1}}{C_{r2}} - 1\right)uu\right] \cdot \frac{\partial}{\partial r_c} f$$

where the coefficients C_{r1} and C_{r2} are given by:

$$C_{r1} = 1 + 8h\ln N + 8h(\ln 2 - 1)$$

$$C_{r2} = 1 + 4h\ln N + 4h(\ln 2 - 1)$$

In the limit of large N, the analytical expressions derived above provide a useful alternative to the algebraic methods described in Appendix A.

For a multibead-rod molecule of 100 beads and for $h = 0.25$, the coefficients for the uu component in the equation of motion for r_c differ only by about 20% when calculated using the Risemann-Kirkwood approximation or calculated according to the Bird-Curtiss approach of Appendix A. In the Risemann-Kirkwood approximation, for very large N the diffusion in the direction parallel to the rod axis is twice that in the direction perpendicular to it; note, however, that this limit is reached slowly (because of the logarithms in the expressions for C_{r1} and C_{r2}).

Manuscript received June 18, 1991, and revision received Dec. 3, 1991.